



Using LIDAR and SNOTEL Data for Evaluating the Performance of Snow Water Equivalent Retrieval Using Sentinel-1 Repeat-Pass Interferometry

Shadi Oveisgharan¹, Emre Havazli¹, Robert Zinke¹, and Zachary Hoppinen²

¹Jet Propulsion Laboratory, California Institute of Technology, 4800 Oak Grove Dr, Pasadena, CA, USA

²Boise State University, Department of Geosciences, 1295 University Drive, Boise, ID, USA

Correspondence: Shadi Oveisgharan (Shadi.Oveisgharan@jpl.nasa.gov)

Abstract. Accurate estimation of snow water equivalent (SWE) at high spatial and temporal resolution remains a critical challenge for hydrologic prediction and climate monitoring. Interferometric Synthetic Aperture Radar (InSAR) provides a promising approach for retrieving SWE by exploiting phase changes induced by snow accumulation. In this study, we evaluate the performance of Sentinel-1 repeat-pass interferometry for SWE retrieval using airborne LIDAR snow depth data and in situ SNOTEL SWE observations across diverse snow climates in the western United States. Using six-day Sentinel-1 acquisitions collected during the NASA SnowEx campaigns of 2020 and 2021, we compare retrieved SWE against independent datasets to quantify retrieval accuracy and assess the influence of environmental factors. Results show that retrievals using six-day repeat pass data yield strong agreement with LIDAR measurements, with Pearson correlation coefficients ranging from 0.42 to 0.66, while 12-day repeat pass data exhibit poor performance due to temporal decorrelation and phase ambiguity. Comparisons with SNOTEL SWE change indicate correlations up to 0.81 and RMSE as low as 0.78 cm. Analysis of retrieval drivers reveals that temporal coherence is the dominant control on performance, followed by temperature, snow wetness, and vegetation cover. Coherence declines with increasing snow depth, slope, and temperature, but improves under dry, cold conditions and gentle terrain. These findings demonstrate that C-band Sentinel-1 InSAR can successfully retrieve SWE change under dry-snow, high-coherence conditions, and highlight the potential of currently in-orbit missions such as NASA-ISRO NISAR to enable global SWE monitoring with improved temporal sampling and wavelength sensitivity.

1 Introduction

Seasonal snowpacks serve as a critical component of the global water cycle, storing and releasing freshwater that supports billions of people worldwide (Barnett et al., 2005). In snow-dominated watersheds, snowmelt is the principal driver of stream-flow and groundwater recharge (Li et al., 2017; Lorenzi et al., 2024), supplying water resources for more than one-sixth of the global population. However, rising temperatures are reducing the likelihood of snowfall in regions historically dominated

by snow (Klos et al., 2014; McCrystall et al., 2021), shifting snow accumulation toward higher elevations and more poleward latitudes. This transition has already decreased the predictability of streamflow in many basins (Siirila-Woodburn et al., 2021).

Accurately mapping SWE at large scales and high spatial resolution is therefore critical for hydrologic forecasting, water management, and climate assessment. SWE, defined as the depth of water obtained if the snowpack were completely melted, has been identified as a key terrestrial variable in NASA's Decadal Survey. Yet, obtaining SWE measurements with sufficient accuracy and resolution remains a persistent challenge. Ground-based networks, such as SNOTEL in the United States (Fleming et al., 2023), provide valuable time series of snow conditions but suffer from limited spatial coverage, elevation bias, and high local variability (Dozier et al., 2016). Passive microwave sensors, which estimate SWE from microwave emissions (Takala et al., 2011; Kelly et al., 2003; Pulliainen and Hallikainen, 2001; Kelly, 2009), supply long-term global records but at coarse spatial resolutions (~ 10 km) and tend to saturate for SWE values above about 150 mm, limiting their applicability in mountainous terrain. Although these systems remain the operational standard for global SWE retrievals, products such as GlobSnow omit mountainous areas because of these resolution and sensitivity constraints.

Airborne LIDAR has proven effective for mapping snow depth at high spatial resolution (Painter and et al., 2016). However, its reliance on clear-sky conditions and limited spatial coverage restrict its ability to provide consistent regional or global observations. There is currently no viable path toward a spaceborne LIDAR system capable of providing global snow depth mapping at the temporal resolution needed for hydrologic applications.

Active microwave sensors, in contrast, offer all-weather capability, high spatial resolution, and global coverage, enabling SWE estimation from spaceborne platforms (Cui et al., 2016; Leinss et al., 2014, 2015; Oveisgharan and Zebker, 2007; Lemmetyinen et al., 2018; Yueh et al., 2017, 2021; Conde et al., 2019; Liu et al., 2017; Eppler et al., 2022; Dagurova et al., 2020; Nagler et al., 2022; Engen et al., 2004; Larsen et al., 2005; Lievens et al., 2019; Belinska et al., 2024). SWE can be retrieved from radar backscatter intensity, which is sensitive to snow depth and microstructure (Rott et al., 2010; Ulaby and Stiles, 1980; Cui et al., 2016; Nghiem and Tsai, 2001; Lievens et al., 2019).

Dual-frequency (X- and Ku-band) SAR missions have been a major focus for future SWE retrieval efforts by the European Space Agency (ESA) and the Canadian Space Agency (CSA) (Rott et al., 2010; Lemmetyinen et al., 2018). However, accurate SWE estimation from radar backscatter remains highly dependent on a priori knowledge of snow micro-structural parameters, particularly grain size (Lemmetyinen et al., 2018; Durand and Liu, 2012; Cui et al., 2016). Recently, the ratio of cross-polarized to co-polarized Sentinel-1 backscatter has been used to estimate snow depth in mountainous regions with deep snow (Lievens et al., 2019, 2022). Nevertheless, the retrieval performance is not yet well quantified (Hoppinen et al., 2024b).

The phase change of specularly reflected radar signals from the snow-ground interface has been shown to depend strongly on variations in SWE for dry snow conditions (Leinss et al., 2015; Guneriusson et al., 2001; Ruiz et al., 2022). In contrast, for wet snow, the phase center is typically located at the snow surface, and the observed phase change is primarily related to snow depth variations (Yueh et al., 2017, 2021; Shah et al., 2017). The underlying principle of this approach is analogous to repeat-pass interferometry, which forms the basis of the SWE retrieval method used in this study and is described in detail in Section 2. A key advantage of the interferometric approach is that SWE retrieval is largely insensitive to snowpack stratigraphy (Yueh et al., 2017) and does not require prior knowledge of snow micro-structural properties.



As detailed in the following sections, the interferometric phase difference between two SAR acquisitions is proportional to small variations in SWE (ΔSWE). Section 2 outlines the retrieval methodology, while Section 3 describes the datasets used in this analysis. In Section 4, we compare the retrieved SWE with coincident airborne LIDAR and in situ SNOTEL observations and assess the influence of environmental parameters on retrieval performance in section 5. This study further demonstrates the potential of InSAR for quantitative SWE estimation and identifies the conditions under which retrieval accuracy is maximized. The methodology developed here is also directly applicable to the new generation L- and S-band missions such as NASA-ISRO's NISAR and ESA's ROSE-L, which will provide suitable observation for global SWE monitoring.

2 SWE Retrieval Using Interferometric Phase

Differential SAR interferometry has been widely used to detect centimeter- to millimeter-scale surface elevation changes across large areas (Gabriel et al., 1989; Zebker et al., 1994). The measured interferometric phase difference is highly sensitive to small variations in SWE (ΔSWE) during the snow season (Gunteriusen et al., 2001; H. Rott and Scheiber, 2003; Deeb et al., 2011; Leinss et al., 2015; Conde et al., 2019; Liu et al., 2017; Hui et al., 2016; Nagler et al., 2022; Eppler et al., 2022; Dagurova et al., 2020; Marshall et al., 2021; Oveisgharan et al., 2024; Hoppinen et al., 2024a; Bonnell et al., 2024b; Ruiz et al., 2022; Tarricone et al., 2023). The technique offers a major advantage in its conceptual simplicity and reduced dependence on a priori snowpack parameters.

For terrestrial snow, the contribution of volume scattering to the interferometric phase is minimal compared to the strong ground return at high radar frequencies. Changes in SWE primarily alter the path delay of the radar signal due to the snow's refractive index. This delay can be quantified through differential interferometry, allowing ΔSWE to be estimated directly from the interferometric phase change (Gunteriusen et al., 2001; Leinss et al., 2015; Conde et al., 2019; Liu et al., 2017; Nagler et al., 2022). Similar to dual-polarization dual-frequency retrieval approaches, this method requires dry snow conditions to ensure penetration to the ground surface.

Retrieval performance can be further improved by combining interferometric phase with backscattered intensity to account for variations in surface roughness (Dagurova et al., 2020). Phase sensitivity to topographic gradients has also been used to help constrain unwrapping errors (Eppler et al., 2022). Although higher radar frequencies increase phase sensitivity to SWE changes, they also amplify decorrelation and unwrapping challenges (Belinska et al., 2024). Multi-frequency approaches can mitigate these issues, improving phase continuity at lower frequencies such as L-band (Belinska et al., 2024).

Recent airborne and satellite experiments have validated the effectiveness of InSAR-based SWE retrieval. Airborne campaigns over the Austrian Alps showed agreement between InSAR-derived SWE and in situ observations, with RMS differences of 4.0 mm and 11.2 mm for snowstorms of 14 mm and 66 mm depth at C- and L-band, respectively (Nagler et al., 2022). Over Grand Mesa, Colorado, L-band UAVSAR ΔSWE retrievals between February 1–13, 2020 correlated strongly with LIDAR-derived snow depth changes under dry conditions (Marshall et al., 2021). Similarly, Sentinel-1 interferometric data yielded a mean SWE accuracy of 6 mm over Finland from only two passes (Conde et al., 2019). Comparisons between L-band InSAR



SWE change and terrestrial LIDAR or GPR observations showed correlations of 0.72–0.79 and RMSE values of 19–22 mm (Bonnell et al., 2024b), with retrieval accuracy decreasing under dense forest cover (Bonnell et al., 2024a).

These studies demonstrate the strong potential of InSAR for SWE estimation, though most were limited in spatial or temporal coverage. Oveisgharan et al. extended these findings by analyzing a long Sentinel-1 time series from winter 2021, validated against extensive in situ measurements and airborne LIDAR (Oveisgharan et al., 2024). They reported a Pearson correlation greater than 0.47 between LIDAR-derived snow depth and retrieved SWE. The correlation and RMSE between retrieved SWE change and in situ station measurements were 0.8 and 0.93 cm, respectively. With the launch of the NASA–ISRO SAR (NISAR) mission, further advances in understanding and operationalizing InSAR-based SWE retrieval are anticipated.

2.1 Retrieving ΔSWE Using Sentinel-1 Data

As described in Section 2, interferometric phase measurements are used to estimate changes in snow water equivalent (SWE). Following the formulation in Oveisgharan et al., the SWE change between two Sentinel-1 acquisitions is expressed as (Oveisgharan et al., 2024):

$$\Delta\phi = -2\kappa_i(-0.3385\theta^2 + 0.0486\theta - 0.8647)\Delta\hat{SWE} \quad (1)$$

where $\Delta\phi$, κ_i , ΔSWE , and θ are interferometric phase between two observation dates, incidence wavenumber, SWE change, and incidence angle, respectively. Temporal coherence is generally low at C-band; however, the 6-day Sentinel-1 repeat cycle significantly improves coherence compared to the nominal 12-day repeat, particularly over snow-covered regions. Consequently, SWE retrievals were primarily performed for areas with available 6-day repeat data, as discussed in section 4. Equation 1 is valid for dry-snow conditions (Leinss et al., 2015; Oveisgharan et al., 2024). Near-surface air temperature exceeding $0^\circ C$ was therefore used as an indicator of wet snow, where this assumption does not hold.

A critical step in ΔSWE estimation is selecting a suitable reference point for phase calibration. In InSAR-based geophysical studies, this point is typically a stable target with negligible or known displacement between acquisitions. Following Oveisgharan et al., we used the average of one or two in situ ΔSWE measurements exhibiting a correlation above 0.35 and subzero temperatures throughout the time series as the reference point for phase calibration (Oveisgharan et al., 2024). Note that reference point selection does not affect comparisons between retrieved total SWE and LIDAR-derived snow depth, since it only introduces a constant phase offset across all dates, preserving spatial variability.

Atmospheric phase delays were estimated using the European Center for Medium-Range Weather Forecasts (ECMWF) ERA5 reanalysis product, which provides hourly atmospheric variables on a 30 km global grid. The Python-based Atmospheric Phase Screen (PyAPS) tool (Jolivet et al., 2011) was used to interpolate these data and convert them into radar phase delays. PyAPS is integrated into the Miami InSAR Time-Series software in Python (Yunjun et al., 2019), which was used to crop the delays to the interferogram extent and project them into the radar line-of-sight (LOS). Ionospheric errors at C-band are small relative to other uncertainty sources and were therefore considered negligible. Phase ambiguity for Sentinel-1 data ranges from approximately 1.5 cm to 3.5 cm, depending on incidence angle (Oveisgharan et al., 2024), making it one of the dominant error sources during large snowstorms associated with significant ΔSWE .



2.2 Temporal Coherence

The radar signals acquired on two different dates remain correlated if the scattering elements within a resolution cell remain unchanged. In practice, however, temporal variations in scatterers—such as the movement of leaves, branches, or snow particles—reduce this correlation, leading to temporal decorrelation (Zebker and Villasenor, 1992; Kellndorfer et al., 2022; Laval-
 125 et al., 2012). Loss of temporal coherence is one of the principal limitations for SWE retrieval using differential interferometry, as discussed in Section 5.1.

In snow-covered regions, melting and wind are the dominant factors that cause decorrelation (Leinss et al., 2015; Luzi et al., 2009). Temporal coherence also decreases with increasing radar frequency (Leinss et al., 2015; Nagler et al., 2022; Kellndorfer
 130 et al., 2022; Ruiz et al., 2022), making longer wavelengths such as L- and C-band more suitable for differential interferometric applications. Vegetation cover can further degrade temporal coherence, particularly at higher frequencies (Baduge et al., 2016; Kellndorfer et al., 2022; Ruiz et al., 2022). Ruiz et al. conducted tower-based fully polarimetric InSAR experiments at L-, S-, C-, and X-bands to assess the effects of air temperature, precipitation, and wind on temporal decorrelation, identifying temperature as the most influential variable (Ruiz et al., 2022). In this study, we extend this analysis using a larger spatial and
 135 temporal dataset to evaluate the effects of multiple environmental and surface parameters on temporal coherence, as discussed in Section 5.

3 Datasets

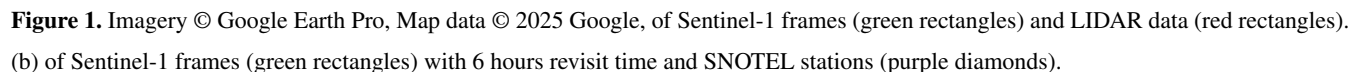
As mentioned in section 2, we use Sentinel-1 data to retrieve SWE. In order to evaluate the performance of our retrievals, we use available LIDAR snow depth and SWE from in-situ stations.

140 3.1 Sentinel-1

Sentinel-1 is a C-band radar mission with four imaging modes, providing resolutions down to 5 m and swath widths up to 400 km. It offers dual polarization, a 12-day repeat cycle, and rapid data access, with products freely distributed through the Alaska Satellite Facility (ASF). Differential interferometric phase and coherence from VV and VH polarizations can be generated globally at 12-day intervals using ASF's On-Demand Processing system. Interferometric processing is supported by the
 145 Hybrid Pluggable Processing Pipeline (HyP3), which applies topographic phase and geolocation corrections and employs the Minimum Cost Flow (MCF) algorithm for phase unwrapping. In this study, we employed the unwrapped phase and interferometric coherence derived from Sentinel-1 observations. The constellation consists of two satellites, each with a 12-day global repeat cycle; when operated in tandem, the effective revisit interval decreases to six days over selected regions, particularly across Europe.

150 The NASA SnowEx2020 and 2021 Time Series represents a continuation of the multi-year initiative to advance snow water equivalent (SWE) measurement and estimation. Data acquisition during winter 2020 and 2021 included multiple sensors (e.g., radar and LIDAR) and in situ collections. As part of this effort, the SnowEx campaign collaborated with the Sentinel-1 team to

Airborne LIDAR provides high-resolution snow depth maps and serves as a reliable source of validation data, offering a particularly strong constraint for InSAR-based retrieval of SWE. For this study, we surveyed all publicly available LIDAR datasets and selected those collected during the snow accumulation season. The "SnowEx20-21 QSI LIDAR DEM 0.5m" dataset, part of the SnowEx 2020 and 2021 campaigns, includes digital elevation models, snow depth, and vegetation height at 5 m spatial resolution (Adebisi et al., 2022). These data were acquired over sites in Colorado, Idaho, and Utah during February 2020, March 2021, and September 2021. In addition, the Airborne Snow Observatory (ASO) program has collected LIDAR observations across the western United States for over seven years, providing snow depth measurements with decimeter-level accuracy and 3 m spacing (DEEMS et al., 2013; Painter et al., 2016). While ASO campaigns are primarily conducted during the melt season—when the timing and magnitude of snowmelt are of critical importance to hydrologic science and water resource management in mountainous regions—some acquisitions are available from the dry snow season. For this analysis, we incorporated all ASO data collected between January and March that were publicly available through their data portal.



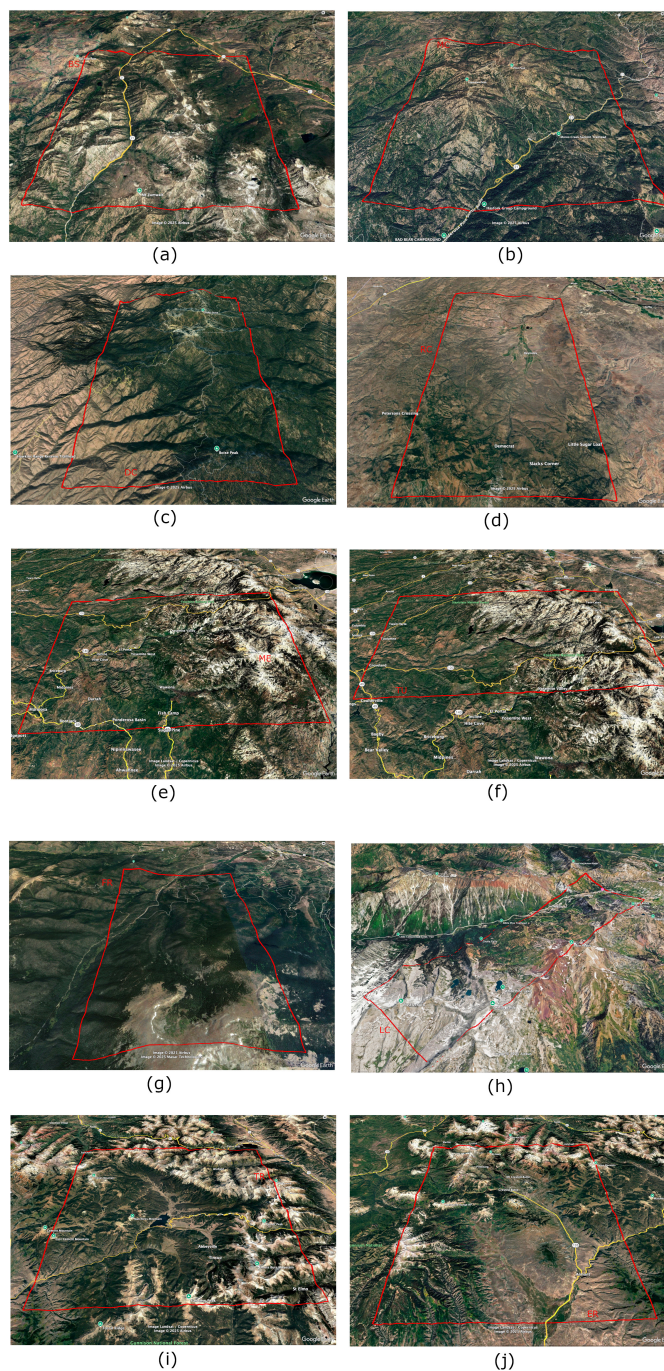


Figure 2. Imagery © Google Earth Pro, Map data © 2025 Google, of LIDAR scenes (a) Banner Summit, ID (b) Mores Creek, ID (c) Dry Creek, ID (d) Reynolds Creek, ID (e) Merced, CA (f) Tuolumne, CA (g) Fraser, CO (h) Little Cottonwood Canyon, UT (i) East River, CO (j) Taylor River, CO



170 As mentioned LIDAR snow depth data is a very valuable dataset for validating our retrieved SWE. The red boxes in figure 1(a) show the location of LIDAR data acquisition during the dry snow regions.

Figure 2 (a)–(j) show the zoomed Google Earth View of LIDAR scenes, Banner Summit, ID (BS), Mores Creek, ID (MC), Dry Creek, ID (DC), Reynolds Creek, ID (RC), Merced, CA (ME), Tuolumne, CA (TU), Fraser, CO (FR), Little Cottonwood Canyon, UT (LC), East River, CO (ER), Taylor River, CO (TR), respectively.

Table 1. Information about LIDAR scenes used in this study. First column shows the site ID. The second column shows the company collecting the data. The third column shows the LIDAR acquisition date. Columns four and five show the revisit time and path/frame of Sentinel-1 time series covering the LIDAR scene, respectively. Last column show the correlation between LIDAR snow depth and retrieved SWE using Sentinel-1 data.

Site ID	LIDAR Sensor	LIDAR Date	Sentinel-1 Revisit Time	Sentinel-1 Path/Frame	Correlation
BS20	QSI	02/19/20	6 days	71/444	0.59
BS21	QSI	03/21/21	6 days	71/444	0.47
MC20	QSI	02/09/20	6 days	71/444	0.66
MC21	QSI	03/15/21	6 days	71/444	0.59
DC20	QSI	02/19/20	6 days	71/444	0.56
RC20	ASO	02/18/20	6 days	71/450	0.44
ME21	ASO	03/26/21	6 days	42/466	0.42
TU21	ASO	02/24/21	6 days	42/466	0.13
FR20	QSI	02/11/20	12 days	56/460	-0.08
LC21	QSI	03/18/21	12 days	100/456	-0.04
ER20	ASO	02/14/20	12 days	56/465	-0.1
TR20	ASO	02/20/20	12 days	56/465	0.08

175 Table 1 summarizes all LIDAR scenes used in this study, consisting of data collected between January and March of 2020 and 2021. The first column lists the LIDAR site ID, followed by the data provider in the second column. The third column reports the date of LIDAR acquisition, while the fourth and fifth columns provide the revisit time and the corresponding



Sentinel-1 path/frame information for the time series covering each LIDAR scene. The LIDAR data are subsequently used in Sections 4.1 and 5.1 to evaluate the performance of SWE retrievals derived from Sentinel-1 observations.

180 3.3 SNOTEL

The SNOWpack TELEmetry (SNOTEL) network consists of stations located in remote, high-elevation mountain regions across the western United States. These stations automatically record a range of snowpack and meteorological variables. For this study, hourly SNOTEL observations were accessed through the United States Department of Agriculture (USDA) website (<https://wcc.sc.egov.usda.gov/nwcc/inventory>). Because we used descending Sentinel-1 acquisitions, collected at approxi-
185 mately 6 a.m. local time, we extracted SNOTEL measurements of SWE, snow depth, and near-surface air temperature corresponding to that time. The locations of the SNOTEL stations are shown as purple diamonds in Figure 1(b). Notably, during winter 2021, only three Sentinel-1 frames with 6 days repeat cycles covered more than five SNOTEL sites. These in situ measurements were employed for (a) establishing InSAR reference points (Section 2.1), (b) evaluating the performance of SWE retrievals (Section 4.2), and (c) analyzing the influence of environmental parameters on SWE retrieval accuracy (Section 5.2).

190 4 Performance of SWE Retrieval Using Sentinel-1 interferometric Phase

In this section, we assess the performance of SWE retrievals derived from Sentinel-1 data. Section 4.1 presents a comparison with LIDAR snow depth measurements, while Section 4.2 evaluates retrieval performance against SNOTEL ΔSWE observations.

4.1 Comparing the Retrieved SWE with LIDAR data

195 As summarized in Table 1 and illustrated in Figures 1 and 2, a total of 10 LIDAR scenes with snow depth measurements were available between January and March of 2020 and 2021. Among these, the Banner Summit (BS) and Mores Creek (MC) sites contain data for both years. For each LIDAR scene, we used the corresponding Sentinel-1 time series (path and frame information provided in Table 1, column 5) to retrieve ΔSWE following the approach described in Section 2. Following Oveisgharan et al. (Oveisgharan et al., 2024), time-series-derived ΔSWE was then used to estimate total SWE at the date
200 closest to the LIDAR acquisition by

$$SWE(t_{i+1}) = \sum_{t_j=t_1}^{t_i} \Delta SWE(t_j, t_{j+1}) \quad (2)$$

where t_1 is the first Sentinel-1 data collected after December first of the corresponding winter and t_{i+1} is the closest Sentinel-1 date to LIDAR acquisition date. For simplicity, we assume the SWE at time t_1 is equal to zero.

To evaluate performance, the analysis was divided into two groups: LIDAR scenes covered by Sentinel-1 data with 6-day
205 revisit intervals and those with 12-day revisit intervals. As shown in Table 1, eight scenes fall into the 6-day repeat group, while four scenes correspond to 12-day repeats.



4.1.1 Using 6-day Repeat Sentinel-1 Data

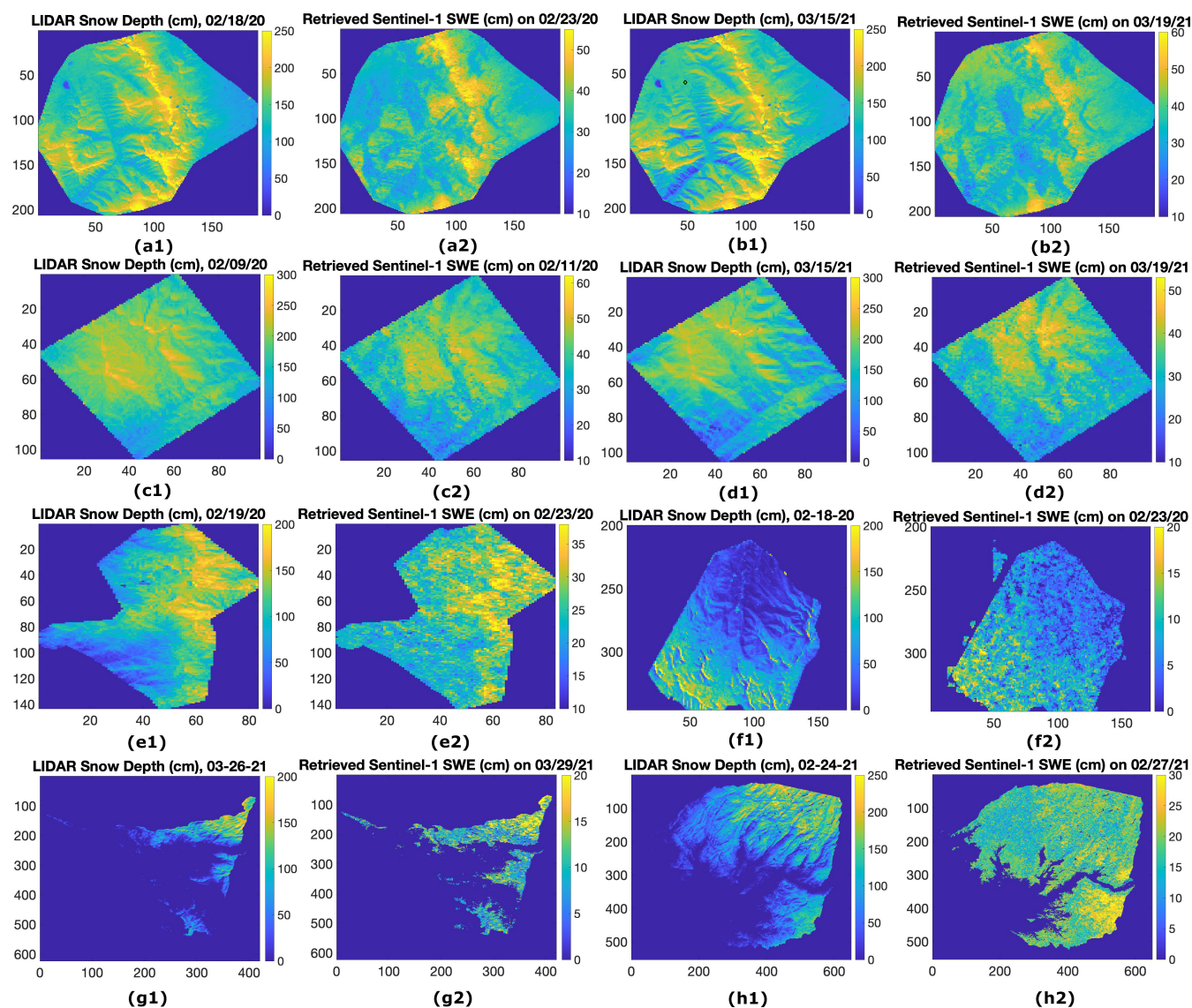


Figure 3. LIDAR total snow depth (a1–h1) for Banner Summit on 02/18/2020, Banner Summit on 03/15/2021, Mores Creek on 02/09/2020, Mores Creek on 03/19/2021, Dry Creek on 02/19/2020, Reynolds Creek on 02/23/2020, Merced on 03/26/2021, and Tuolumne on 02/27/2021, respectively. Images (a2–h2) show the total retrieved SWE using 6 d repeat Sentinel-1 time series data from December 1st to closest date to LIDAR date acquisition, respectively.

Figures 3(a1–h1) present LIDAR-derived snow depth for Banner Summit (02/18/2020 and 03/15/2021), Mores Creek (02/09/2020 and 03/19/2021), Dry Creek (02/19/2020), Reynolds Creek (02/23/2020), Merced (03/26/2021), and Tuolumne



210 (02/27/2021). The corresponding retrieved total SWE, derived from Sentinel-1 6-day time series using Equation 2, is shown in Figures 3(a2–h2). We refer to each LIDAR scene by site abbreviation and year (e.g., BS20 = Banner Summit 2020, MC21 = Mores Creek 2021). For each case, the Sentinel-1 acquisition date closest to the LIDAR survey date (t_{i+1} in Equation 2) is indicated in the figure titles. Overall, the retrieved SWE fields show strong visual agreement with the LIDAR snow depth maps. The Pearson correlation coefficients between LIDAR snow depth and Sentinel-1-derived SWE, reported in the last column of Table 1, range from 0.42 to 0.66 across sites, with the exception of Tuolumne (TU).

215 Within the LIDAR frames shown in Figures 3(a1–h1), all scenes except Merced (Figure 3g1) contain at least one SNOTEL site. Figures 4(a1–h1) present the total SWE time series from these SNOTEL stations, beginning on December 1 of the corresponding winter. Figures 4(a2–h2) show the corresponding near-surface air temperature time series. The dashed vertical lines mark the start dates of each 6-day Sentinel-1 acquisition cycle. Notably, a data gap occurred on February 5, 2021, resulting in a missing six-day repeat acquisition.

220 The correlation between retrieved SWE and LIDAR snow depth varies across sites, with lower values observed for Reynolds Creek (RC) and Merced (ME) compared to Banner Summit (BS), Mores Creek (MC), and Dry Creek (DC). The correlation is particularly weak at Tuolumne (TU). As shown in Figures 4(f1–f2), total SWE and SWE changes between Sentinel-1 acquisitions were minimal for RC20, while temperatures exceeded 0°C on 25 days during the season before LIDAR acquisition date. The presence of wet snow and limited SWE variability degrades retrieval performance (Oveisgharan et al., 2024), explaining the weaker correlation at RC20. Although Merced lacks a co-located SNOTEL site, it is geographically close to TU, and therefore SNOTEL data from the TU frame were used as a proxy. Between December 1 and the corresponding LIDAR acquisition dates, the number of days with above-freezing temperatures at SNOTEL stations was 0, 1, 4, 7, 10, 25, and 16 for BS20, BS21, MC20, MC21, DC20, RC20, and TU21, respectively. These higher temperatures and more frequent melt events in RC, ME, and TU contributed to the reduced correlations between Sentinel-1-derived SWE and LIDAR snow depth. A large snowstorm was also observed at TU, with an SWE increase of 8.89 cm between January 22 and January 28, 2021 (acquisition 9). Although the overall correlation between retrieved SWE and LIDAR snow depth at TU21 was low (0.13), the correlation between LIDAR snow depth and retrieved ΔSWE during this storm (acquisition 9) reached 0.6. This suggests that melt events during other periods were responsible for degrading retrieval performance at TU21.

235 4.1.2 Using 12-day Repeat Sentinel-1 Data

240 Figures 5(a1–d1) present LIDAR-derived snow depth for Fraser (FR20, 02/11/2020), Little Cottonwood Canyon (LC21, 03/18/2021), East River (ER20, 02/14/2020), and Taylor River (TR20, 02/20/2020). The corresponding retrieved SWE, derived using Equation 2 and Sentinel-1 12-day time series, is shown in Figures 5(a2–d2). For each case, the Sentinel-1 acquisition date closest to the LIDAR survey (t_{i+1} in Equation 2) is indicated in the figure titles. Unlike the 6-day repeat results, these scenes show little resemblance between LIDAR snow depth and Sentinel-1-derived SWE. The Pearson correlation coefficients range from -0.1 to 0.08 , confirming that a 12-day revisit interval is too coarse for SWE retrieval using C-band Sentinel-1 data.

Figures 6(a1–d1) display the SNOTEL SWE time series within the LIDAR frames of Figures 5(a1–d1), beginning December 1 of the corresponding winter. The associated near-surface temperature time series are shown in Figures 6(a2–d2). Dashed

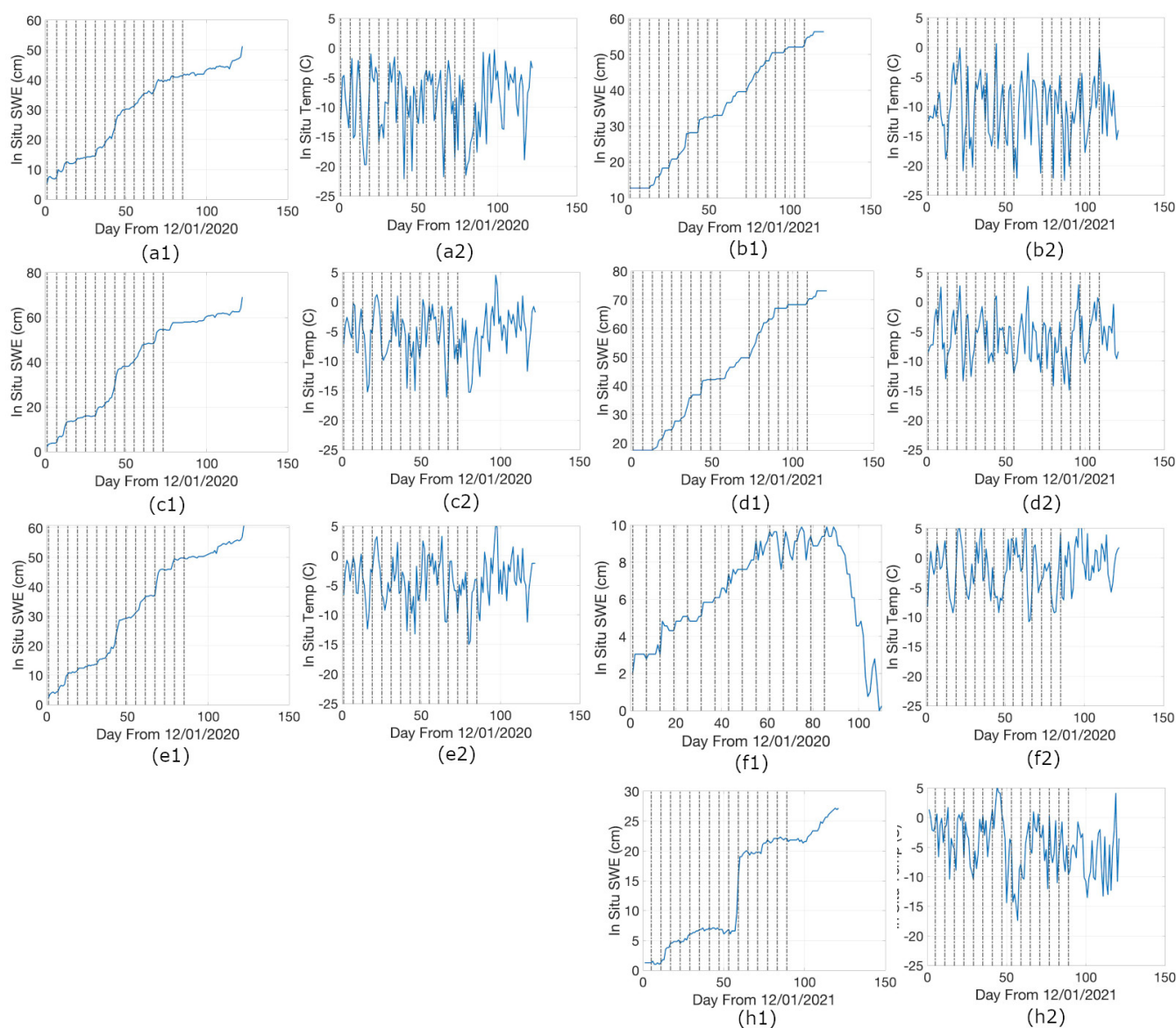


Figure 4. SWE (a1–h1) and Temperature (a2–h2) for SNOTEL stations inside BS in 2020, BS in 2021, MC in 2020, MC in 2021, DC in 2020, RC in 2020, ME in 2021, and TU in 2021, respectively. The dashed vertical lines show the start date of Sentinel-1 observations.

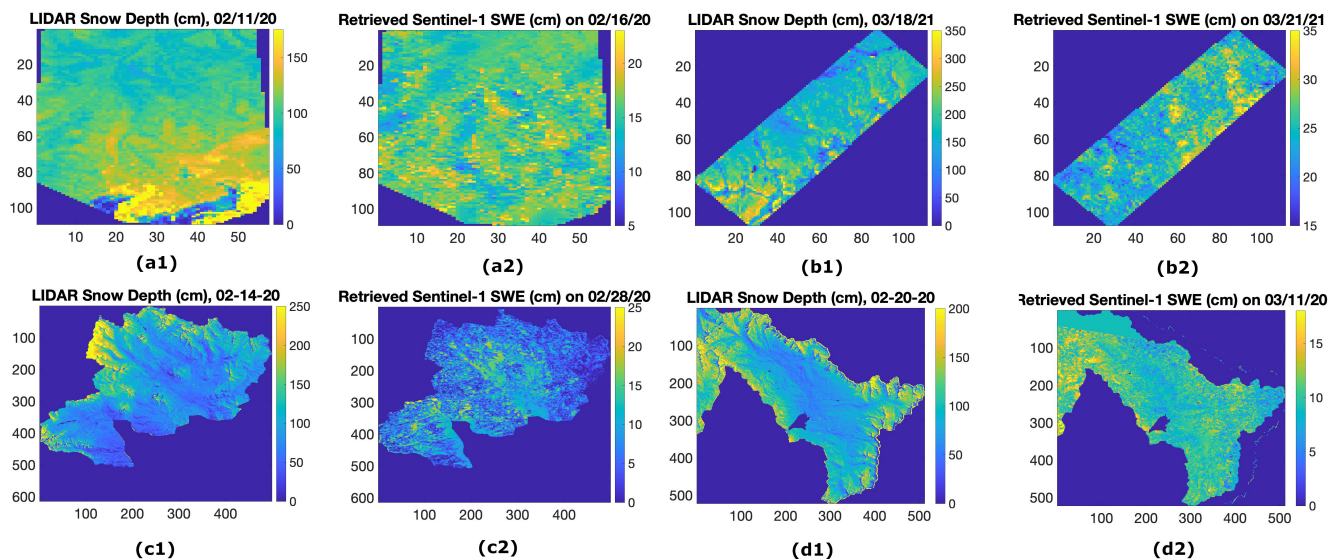


Figure 5. LIDAR total snow depth (a1–d1) for Fraser on 02/11/2020, Little Cottonwood Canyon on 03/21/2021, East River on 02/14/2020, and Taylor River on 03/11/2020. Images (a2–d2) show the total retrieved SWE using 12 d repeat Sentinel-1 time series data from December 1st to closest date to LIDAR date acquisition, respectively.

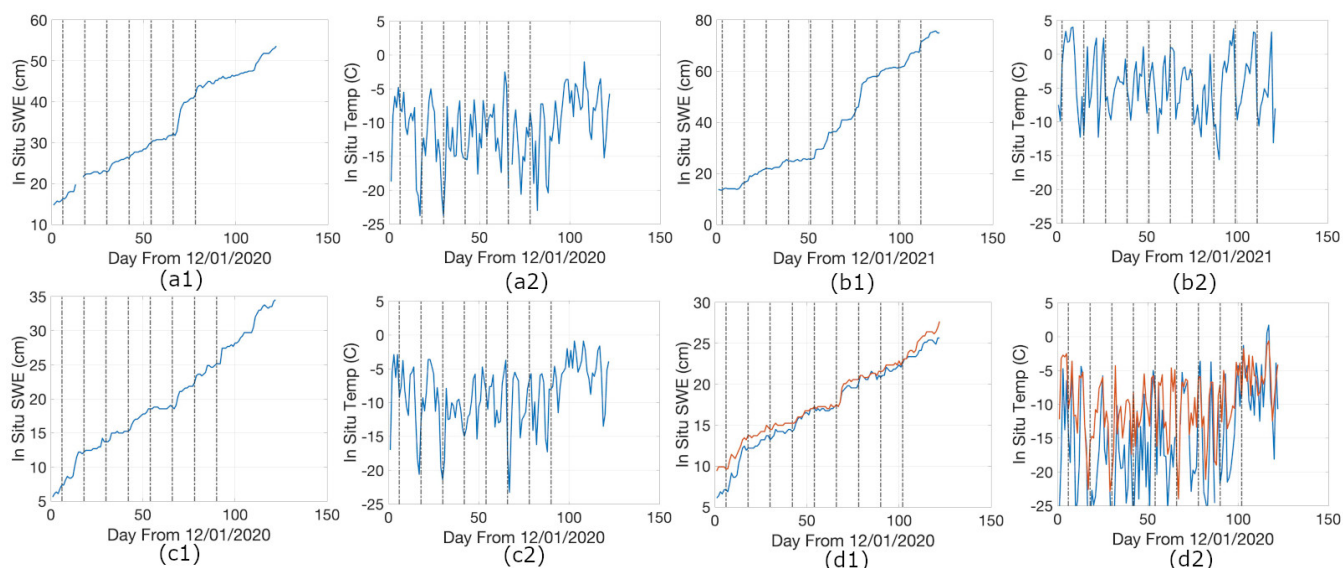


Figure 6. SWE (a1–d1) and Temperature (a2–h2) for SNOTEL stations inside FR in 2020, LC in 2021, ER in 2020, and TR in 2020, respectively. The dashed vertical lines show the start date of Sentinel-1 observations.



vertical lines mark the start dates of each 12-day Sentinel-1 acquisition cycle. The results demonstrate that temporal coherence
 245 degrades significantly at this longer revisit interval, rendering the data unreliable for SWE retrieval. Nevertheless, the SNO-
 TEL SWE and temperature records are later used in Section 5.1 to investigate the environmental factors influencing temporal
 coherence.

4.2 Comparing the Retrieved SWE Using Sentinel-1 with SNOTEL SWE

As described in Section 3.1, Sentinel-1 data were acquired every 6 days over three frames containing more than five SNOTEL
 250 sites (Figure 1b) during 2020 and 2021, coordinated between the SnowEx campaign and the Sentinel-1 team. For this analysis,
 we used 6-day repeat Sentinel-1 time series from 12/01/2020 to 03/30/2021.

The left, middle, and right columns of Figure 7 correspond to frames (p71,f444), (p71,f450), and (p42,f461), respectively.
 Figures 7(a1–c1) show SNOTEL SWE time series from 12/01/2020 to 03/31/2021 at 6:00 am for all stations within each
 frame, with different colors indicating individual SNOTEL sites. SWE increases relatively uniformly in (p71,f444), whereas
 255 sharp increases are observed in (p71,f450) and (p42,f461). Snowpack is also generally shallower in (p71,f450).

Figures 7(a2–c2) present the average near-surface temperature across SNOTEL stations in each frame. Among them,
 (p42,f461) is consistently warmer than (p71,f444) and (p71,f450). Figures 7(a3–c3) display the average Sentinel-1 tempo-
 ral coherence time series, with black squares marking SNOTEL locations. Low-coherence regions align with snow-covered
 areas. Frame (p71,f450) exhibits higher coherence due to its shallower snowpack, while (p42,f461) shows lower coherence
 260 compared to (p71,f444).

Figures 7(a4–c4) compare retrieved ΔSWE from Sentinel-1 time series with ΔSWE from SNOTEL stations over the study
 period. The correlation coefficients are 0.81, 0.55, and 0.54 for frames (p71,f444), (p71,f450), and (p42,f461), respectively.
 The corresponding RMSE values are 0.78 cm, 1.32 cm, and 1.17 cm. The reduced performance in (p71,f450) and (p42,f461)
 is attributed to limited SWE change in the former and warmer temperatures in the latter.

265 5 Impact of Different Parameters on SWE Retrieval

As demonstrated in Sections 4.1 and 4.2, the correlation between Sentinel-1–retrieved SWE or ΔSWE and validation datasets
 (LIDAR snow depth or SNOTEL ΔSWE) varies across sites. In this section, we investigate the key factors influencing these
 correlations.

5.1 Impact of Different Parameters on Retrieved SWE Using LIDAR Data

270 In this section, we assess how various parameters influence the performance of SWE retrieval from Sentinel-1 by comparing
 retrieved SWE against LIDAR snow depth. Performance is quantified using the correlation between the two datasets. The last
 column of Table 1 reports the correlation for each LIDAR scene over the entire image. To further investigate, we partition the
 data according to specific parameters and recompute the correlations.

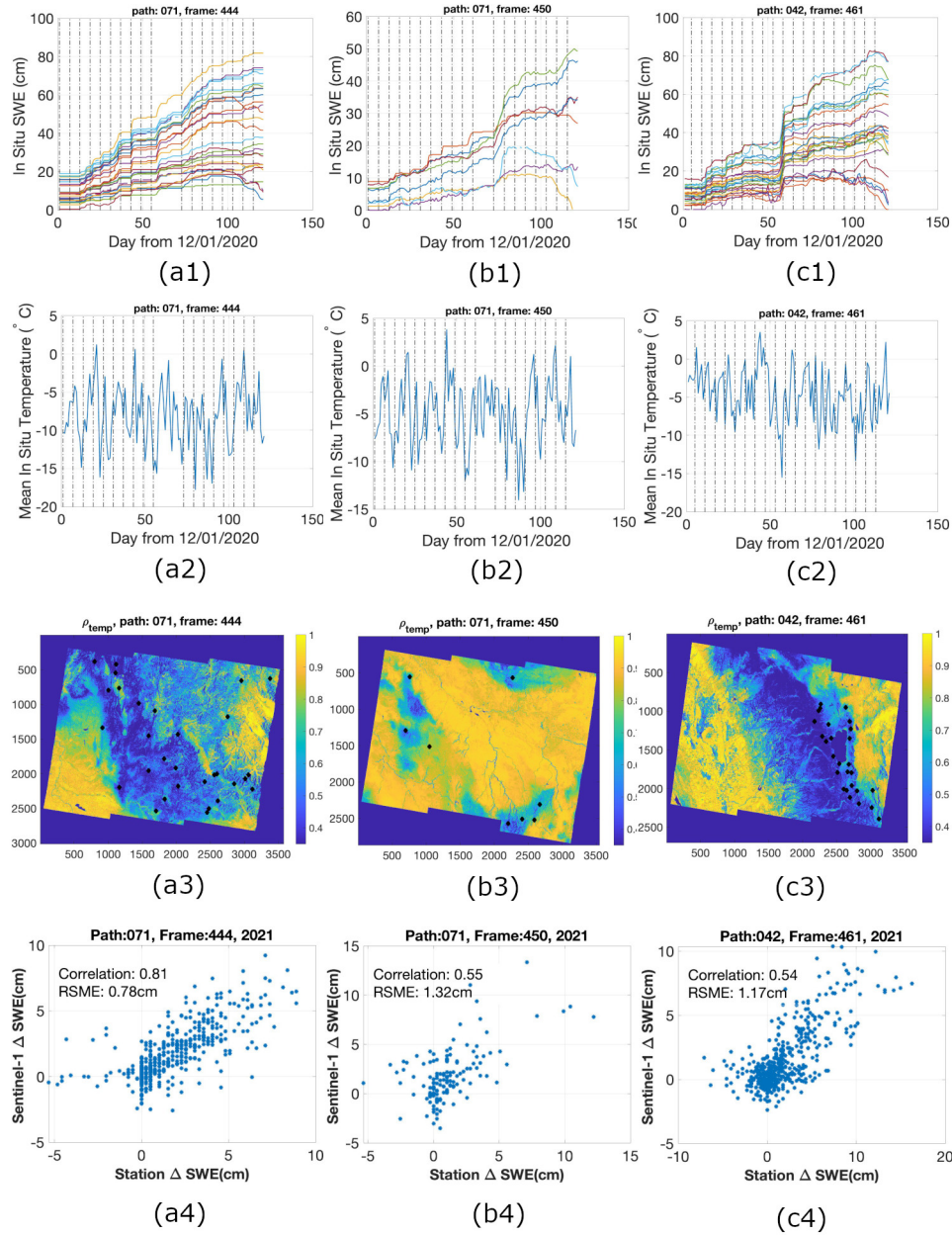


Figure 7. (a1) SNOTEL SWE measurements (cm) for all stations in Sentinel-1 (p71,f444) starting December first to end of March. Different colors show the measurements for different SNOTEL stations. (a2) Mean of all SNOTEL temperature measurements (C) in Sentinel-1 (p71,f444) starting December first to end of March. (a3) Mean of Sentinel-1 temporal coherence for (p71,f444) starting December first to end of March. (a4) Retrieved Δ SWE vs SNOTEL Δ SWE for (p71,f444) every 6 days starting December first to end of March. Figures (b1–b4) and (c1–c4) are the same as Figure (a1–a4), but use Sentinel-1 data from (p71, f450) and (p42, f461), respectively.



Figure 8(a) shows the relationship between correlation and mean Sentinel-1 temporal coherence (ρ_{temp}) for sites with available 6-day repeat acquisitions. Different colors represent different LIDAR sites. As seen in the figure, the correlation generally increases with higher temporal coherence across most sites, with the exception of RC20. For example, in BS21 the overall correlation between retrieved SWE and LIDAR snow depth is 0.47 for the entire image, but ranges from ~ 0.1 at low coherence to ~ 0.78 at $\rho_{temp} \approx 0.75$. This pattern is consistent across most scenes, underscoring the critical role of temporal coherence in SWE retrieval: higher coherence enables more reliable phase measurements and, consequently, more accurate retrievals. Therefore, the impact of different parameters on temporal coherence is evaluated in section 5.1.1.

Although TU21 exhibits a low overall correlation (0.13), Figure 8(a) (blue dashed line) shows that correlation still rises to ~ 0.5 in regions with higher temporal coherence. This demonstrates that reliable retrieval is possible even in generally low-performing sites when coherence is sufficiently high. However, because TU21 has low overall coherence across the scene, we exclude it from the parameter impact analysis. The exception is RC20, where temporal coherence does not improve retrieval performance. As discussed previously, this is likely due to frequent melt events and overall low SWE, which degrade retrieval accuracy despite coherence levels.

Figure 8(b) illustrates the correlation between retrieved SWE time series and LIDAR snow depth at the end of the time series. In most sites, correlations are relatively low early in the snow season but increase steadily, reaching near-maximum values between mid-January and early February, and attaining their highest values at the end of the time series. The fact that maximum correlation occurs at the LIDAR acquisition date indicates that the relationship is not random; rather, the correlation

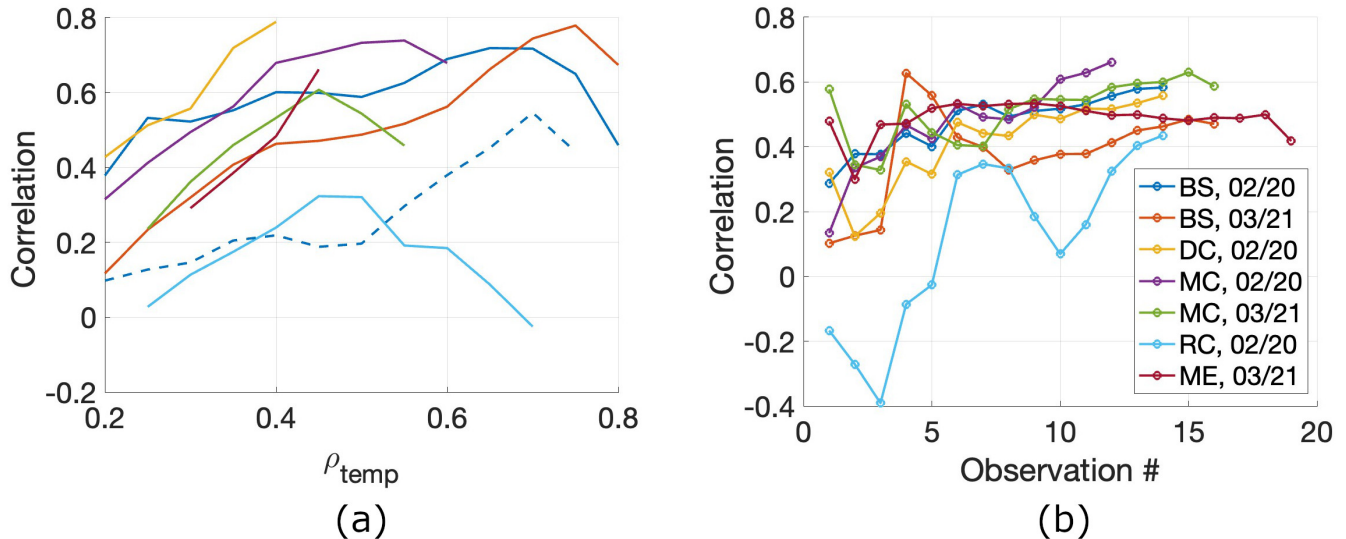


Figure 8. (a) Correlation between retrieved SWE using Sentinel-1 data and LIDAR snow depth versus average of Sentinel-1 temporal coherence. (b) Correlation between LIDAR snow depth and retrieved total SWE using Sentinel-1 on a specific observation date versus observation number. Different colors show the different LIDAR scenes.



strengthens as the retrieval approaches the validation date. This trend also suggests that the primary spatial pattern of snow accumulation is largely established by February.

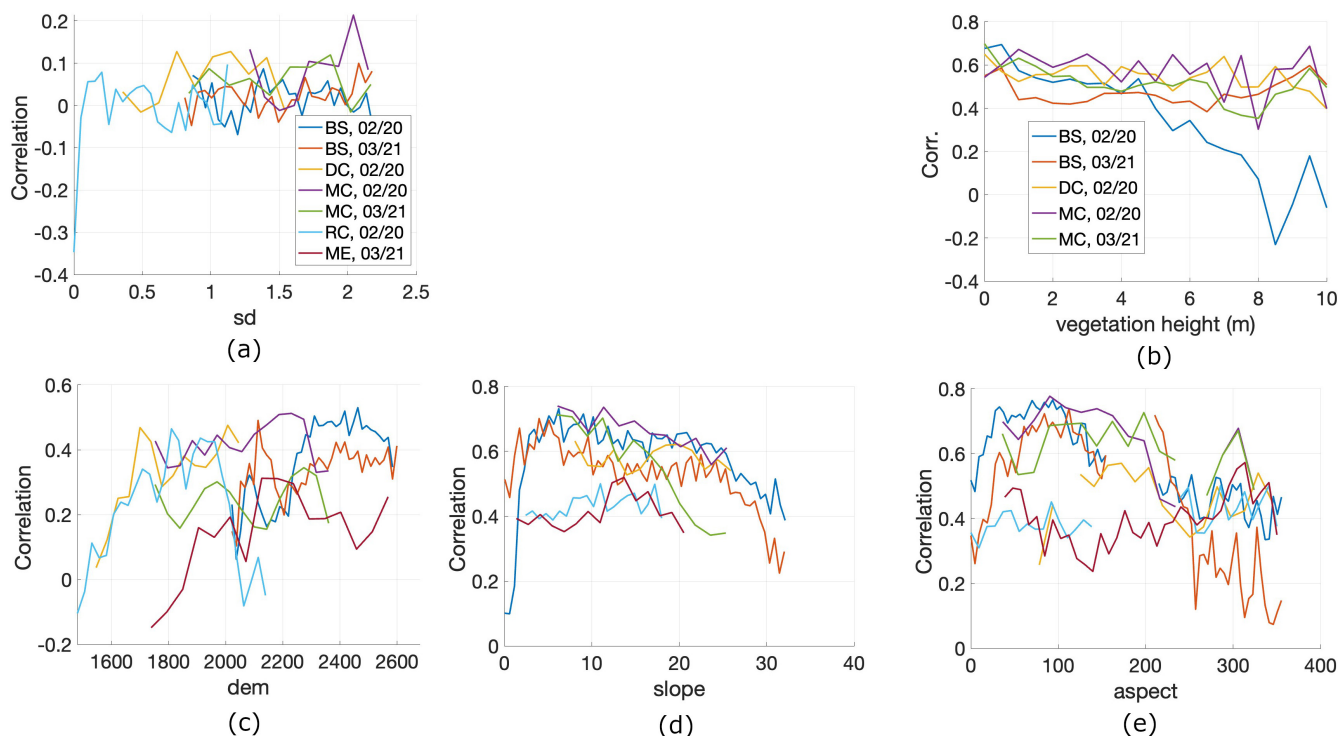


Figure 9. Correlation between retrieved SWE using Sentinel-1 data and LIDAR snow depth versus (a) snow depth (b) vegetation height (c) ground topography (d) ground slope (e) ground aspect. Different colors show the different LIDAR scenes.

Figures 9(a–e) illustrate the influence of snow depth, vegetation height, ground topography, slope, and aspect on the correlation between retrieved SWE and LIDAR snow depth. Different colors represent different LIDAR sites. Vegetation height data are only available for the QSI LIDAR products. As shown in Figure 9(a), total snow depth has little effect on retrieval performance. In contrast, Figure 9(b) demonstrates that correlation decreases with increasing vegetation height, likely because vegetation obscures the snowpack and reduces retrieval accuracy. However, retrievals may remain reliable even in areas with tall vegetation, possibly due to canopy gaps or snow accumulation on top of the canopy. Correlation tends to increase with ground elevation within each site (Figure 9c). However, this relationship is local rather than global; there is no specific elevation threshold beyond which performance improves uniformly. Instead, within a given site, higher elevations generally correspond to colder conditions, leading to drier snow and thus more reliable retrieval.

As shown in Figure 9(d), correlation generally decreases with increasing ground slope, except in RC20 and ME21. Steeper slopes are expected to promote snow displacement, reducing temporal coherence and retrieval performance. However, RC20 and ME21 have relatively shallow snowpacks, which may limit downslope snow movement and explain the lack of slope



dependence. Figure 9(e) shows that correlation is highest (except in RC20 and ME21) for aspect angles near 90° , corresponding to east-facing slopes. A possible explanation is that these slopes receive sunlight earlier in the day, when temperatures are lower, thereby minimizing melt compared to west-facing slopes that receive afternoon sun under warmer conditions. In contrast, RC20 and ME21 exhibit consistently low correlations across all aspect angles, consistent with their shallow snowpack and warmer temperatures.

5.1.1 Impact of Different Parameters on INSAR Temporal Coherence Using LIDAR Data

As discussed in Section 5.1, temporal coherence plays a critical role in SWE retrieval. To further investigate this, we evaluate the influence of different environmental parameters on temporal coherence over the LIDAR scenes. Since retrieval performance is very poor with 12-day repeat Sentinel-1 data, Section 5.1 considered only 6-day repeat acquisitions. Here, we assess parameter impacts separately for 6-day and 12-day repeat data.

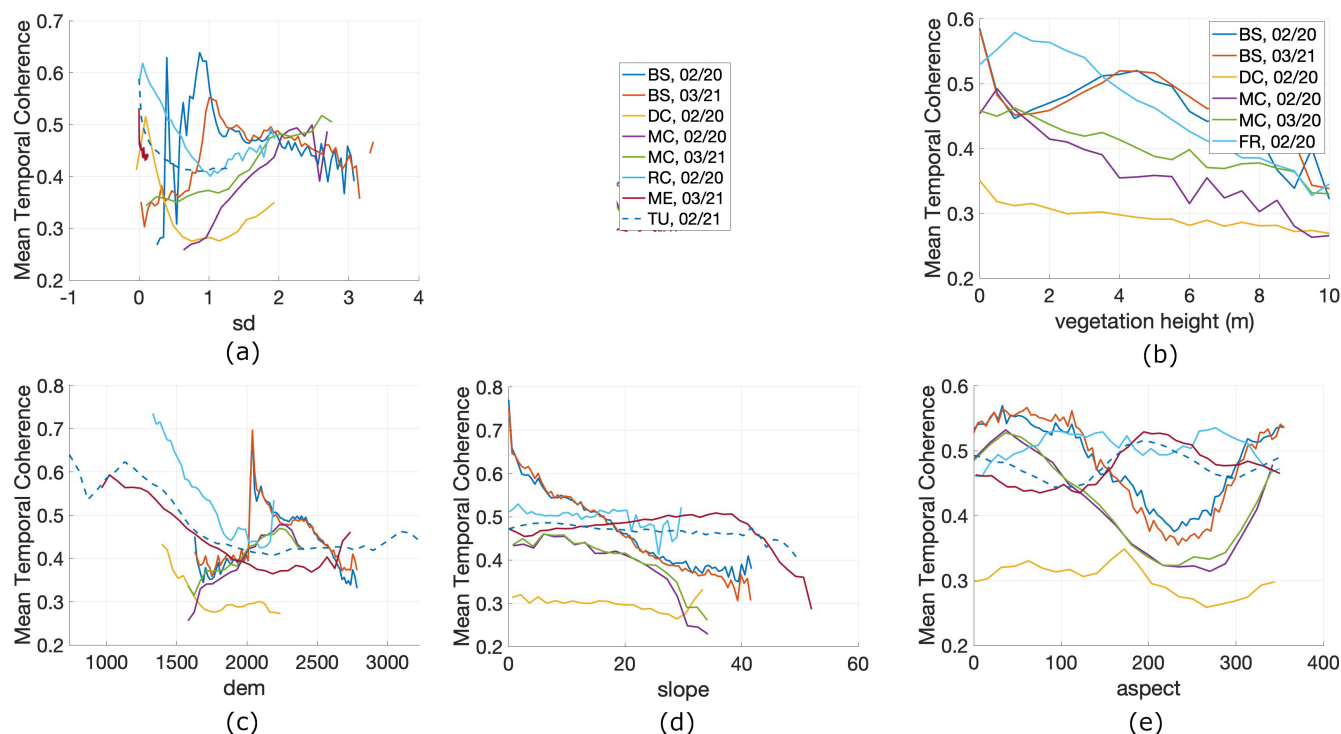


Figure 10. Average of Sentinel-1 temporal coherence versus (a) snow depth (b) vegetation height (c) ground topography (d) ground slope (e) ground aspect. Different colors show the different LIDAR scenes.

Figure 10(a–e) illustrates the effects of snow depth, vegetation height, elevation, slope, and aspect on Sentinel-1 temporal coherence, with different colors representing different LIDAR sites. The Sentinel-1 temporal coherence values shown in Figures 10(a–e) are derived from 6-day repeat acquisitions. As shown in Figure 10(a), increasing snow depth generally reduces



temporal coherence, except at the MC site. Deeper snow typically introduces more movement and structural change, lowering coherence. The anomalous behavior at MC remains unexplained. Notably, snow depth influences temporal coherence, whereas it showed little effect on correlation with LIDAR in Figure 9(a).

Figure 10(b) shows that temporal coherence decreases with increasing vegetation height, likely due to motion of leaves and branches. The impact of vegetation is stronger for temporal coherence than for correlation (cf. Figure 9b). Temporal coherence also tends to decrease with elevation within individual sites (Figure 10c). This relationship is site-specific rather than global: higher elevations often correspond to greater snow depth variability and wind exposure, which reduce coherence. Interestingly, topography exerts opposite effects on correlation and temporal coherence (Figures 9c and 10c): higher elevations improve retrieval accuracy (drier snow) but reduce temporal coherence (increased snow depth change and wind).

As shown in Figure 10(d), coherence generally decreases with slope, consistent with the expectation that steeper terrain promotes snow displacement and reduces stability. RC20 and ME21 are exceptions, likely due to their shallow snowpacks, which limit slope-induced snow movement.

Aspect also plays an important role (Figure 10e). Coherence is generally highest (except in ME21 and TU21) for east-facing slopes ($\sim 90^\circ$) and lowest for west-facing slopes ($\sim 270^\circ$). A possible explanation is that east-facing slopes receive sunlight earlier in the day, under colder conditions, which minimizes melt compared to west-facing slopes that experience warmer afternoon temperatures. By contrast, ME21 and TU21 show the opposite pattern, with higher coherence on west-facing slopes, possibly due to site-specific wind effects.

Figure 11(a–d) illustrates the influence of snow depth, elevation, slope, and aspect on Sentinel-1 temporal coherence using 12-day repeat data. The overall parameter dependencies are consistent with those observed for the 6-day repeat case (Figure 10). However, coherence values are systematically lower for 12-day intervals, indicating that longer revisit times degrade temporal coherence even though the relative effects of the parameters remain similar.

5.2 Impact of Different Parameters on Retrieved SWE Using SNOTEL Data

In this section, we examine how different parameters affect the correlation between Sentinel-1–retrieved and SNOTEL ΔSWE using 6-day repeat acquisitions. We also assess the influence of these parameters on Sentinel-1 temporal coherence.

Figures 12(a–c) illustrate the effects of temporal coherence, temperature, and ΔSWE on the correlation between retrieved and SNOTEL ΔSWE , with different colors representing individual Sentinel-1 frames. For each frame in Figure 1(b), we use the full time series of parameters and calculate the correlation for each subcategory. For example, in Figure 1(b) the correlation between retrieved and SNOTEL ΔSWE is about 0.9 for all SNOTEL observations within the temperature range $-15^\circ C$ to $-10^\circ C$ in (p71,f444).

Figure 12(a) shows that the correlation between retrieved and SNOTEL ΔSWE increases with temporal coherence for (p71,f444), but decreases for (p71,f450) and (p42,f461). This differs from the pattern observed in Figure 8(a) for correlations between total SWE and LIDAR snow depth. One possible explanation is that the error in choice of reference point affects ΔSWE comparison from different dates but not total SWE retrieval. Another explanation could be that higher temporal coherence often corresponds to smaller ΔSWE , and retrieval performance may degrade when SWE changes are small.

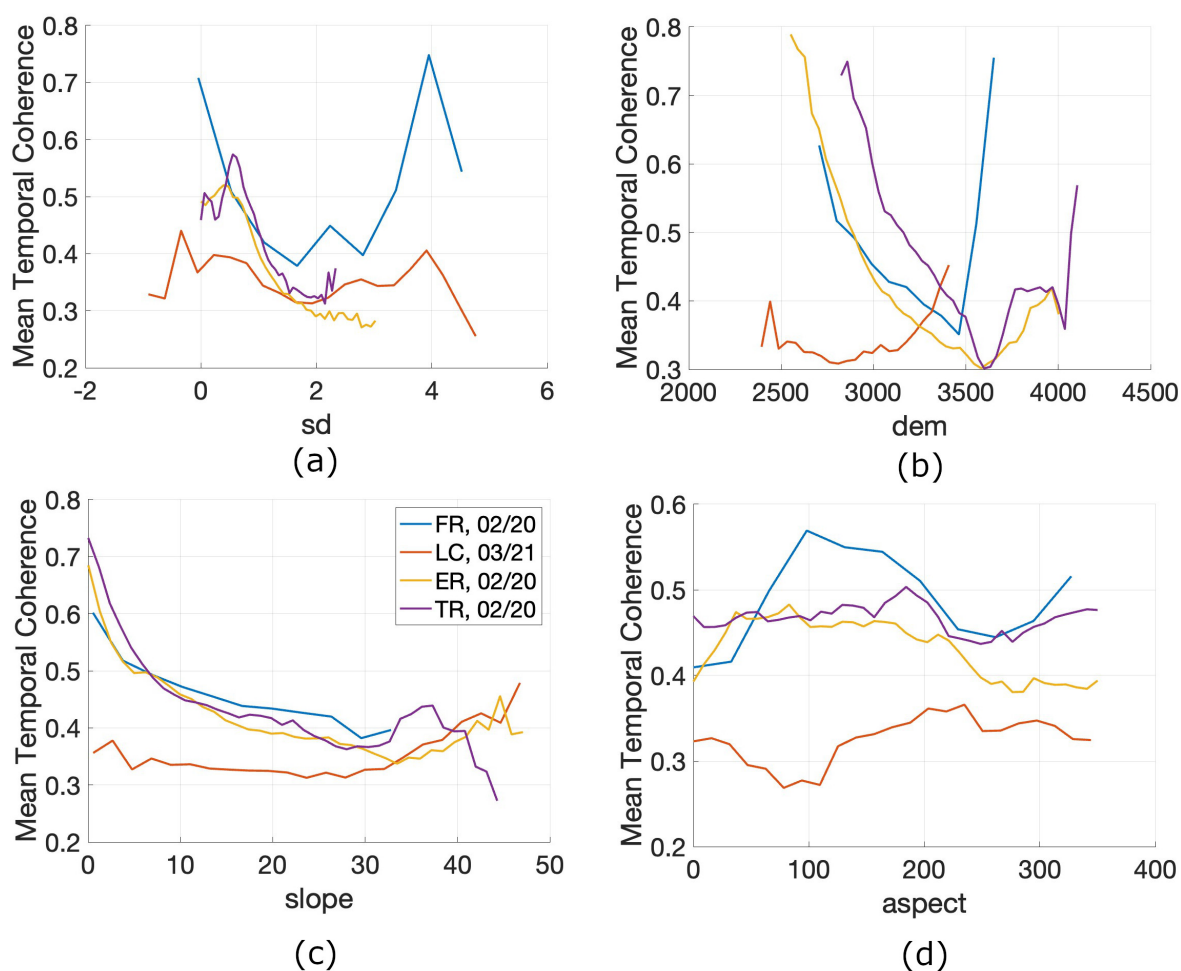


Figure 11. Average of Sentinel-1 temporal coherence versus (a) snow depth (b) ground topography (c) ground slope (d) ground aspect. Different colors show the different LIDAR scenes.



355

As expected, higher temperatures reduce retrieval performance, as shown in Figure 12(b). Warmer conditions promote melt, which lowers the correlation between retrieved and SNOTEL ΔSWE , consistent with the behavior reported in (Ruiz et al., 2022). In contrast, the magnitude of SWE change does not significantly impact correlation, as shown in Figure 12(c).

We also evaluate the influence of temperature and SWE change on temporal coherence using SNOTEL data. Figures 13(a) and 13(b) show that temporal coherence decreases with increasing temperature and with larger ΔSWE . Higher temperatures

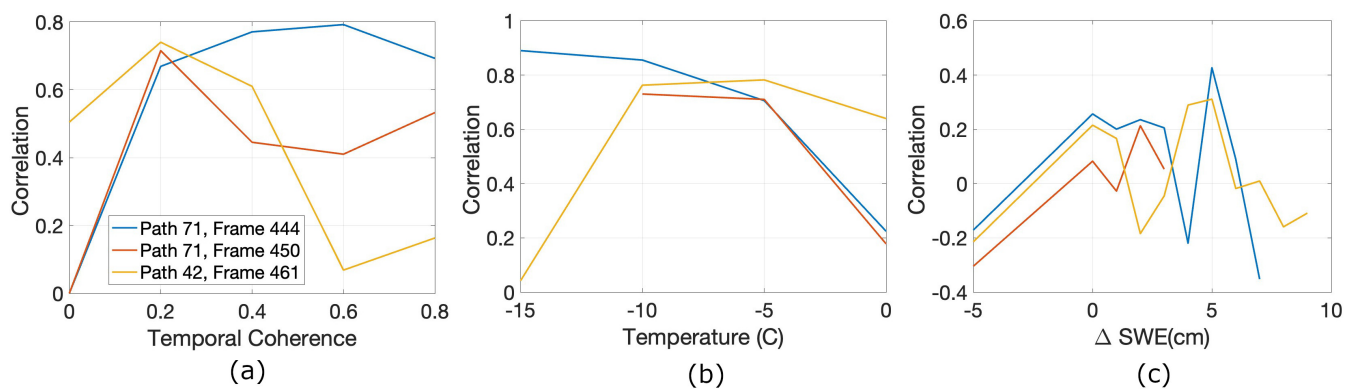


Figure 12. Correlation between retrieved ΔSWE using Sentinel-1 data and SNOTEL ΔSWE versus (a) Sentinel-1 temporal coherence (b) Temperature (C) (c) ΔSWE .

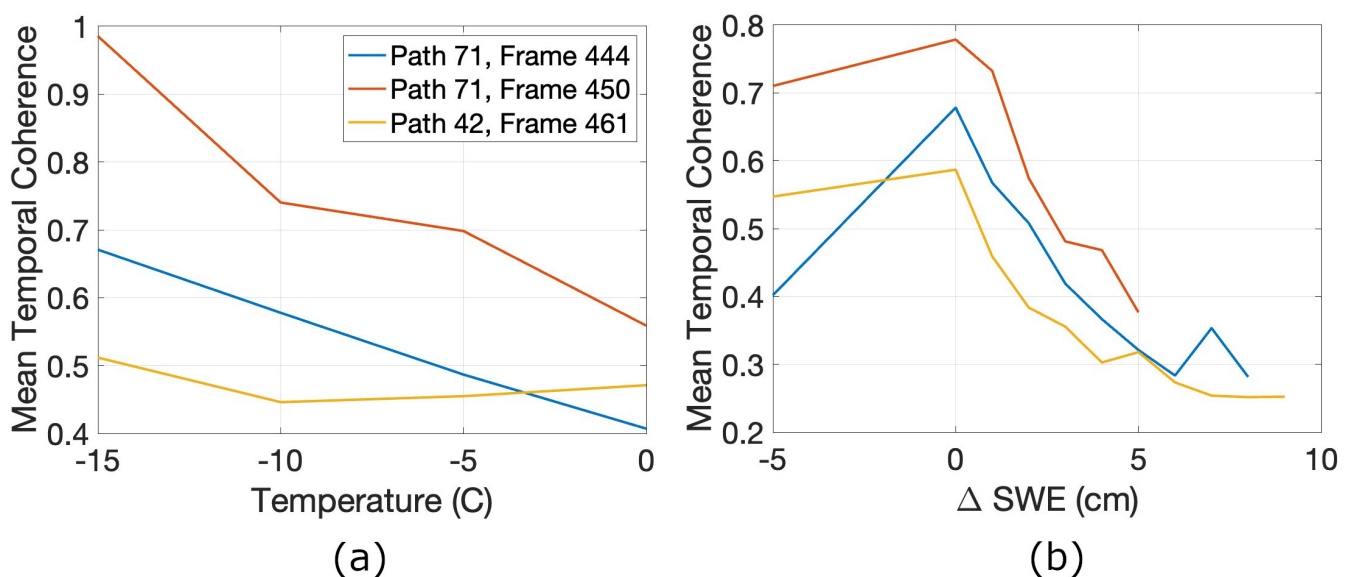


Figure 13. Average of Sentinel-1 temporal coherence versus (a) temperature (C) (b) ΔSWE .



make the snow wetter and increase particle motion, reducing coherence. Similarly, larger SWE changes are often accompanied by strong winds and substantial modifications to the scattering medium, which also degrade temporal coherence.

0

360 6 Conclusions

This study evaluated the performance of Sentinel-1 repeat-pass interferometry for estimating snow water equivalent (SWE) across multiple SnowEx sites using coincident airborne LIDAR and SNOTEL datasets. Results confirm that the 6-day Sentinel-1 acquisitions coordinated with the SnowEx campaign substantially enhance temporal coherence and improve SWE retrieval performance relative to the standard 12-day repeat. The correlation between Sentinel-1-retrieved SWE and LIDAR snow depth
365 ranges from 0.42 to 0.66 across sites, with the strongest agreement observed in cold, dry regions exhibiting stable snowpacks. Similarly, correlations between retrieved and SNOTEL SWE change reach 0.81, with corresponding RMSE values below 1 cm. Our analysis demonstrates that temporal coherence exerts the strongest influence on retrieval accuracy. Coherence decreases with increasing snow depth, slope, vegetation height, temperature, and SWE change, indicating that snow metamorphism, melt events, and surface motion are primary sources of decorrelation. Reliable retrievals are achieved primarily under cold,
370 dry-snow conditions and in relatively flat, sparsely vegetated terrain. While 12-day revisit intervals result in severe coherence loss, the 6-day repeat provides sufficient temporal stability for C-band SWE retrieval in many mountain environments. These findings validate the feasibility of C-band InSAR for quantitative SWE mapping and provide insight into the environmental and observational constraints governing retrieval performance. The framework and analyses developed here directly inform the application of upcoming L- and S-band missions such as NISAR, which will extend InSAR-based SWE retrievals to global
375 scales with improved coherence and temporal sampling.

7 Author contributions

SO conceptualized the study and processed the Sentinel-1 data using HyP3. EH applied the atmospheric corrections, and RZ assisted with atmospheric removal for two Sentinel-1 frames early in the project. ZH conducted initial performance analyses of the SWE retrievals using the Banner Summit LIDAR dataset. SO performed the full analysis and evaluated the SWE retrieval
380 performance statistics. EH contributed valuable discussions and feedback throughout the study.

8 Competing interests

The contact author has declared that none of the authors has any competing interests.



9 Acknowledgments

385 The authors would like to thank NASA Terrestrial Hydrology Program 2024 and JPL R&TD for providing funding for this project. The research was carried out at the Jet Propulsion Laboratory, California Institute of Technology, under a contract with the National Aeronautics and Space Administration (80NM0018D0004). The authors also acknowledge the use of AI-assisted editing tools (ChatGPT, OpenAI) to help improve the clarity and readability of parts of this manuscript.



References

- Adebisi, N., Marshall, H., Vuyovich, C. M., Elder, K., Hiemstra, C., and Durand, M.: SnowEx20-21 QSI Lidar Snow Depth 0.5m UTM Grid, Version 1, <https://doi.org/10.5067/VBUN16K365DG>, 2022.
- Baduge, A. W. A., Henschel, M. D., Hobbs, S., Buehler, S. A., Ekman, J., and Lehrbass, B.: Seasonal variation of coherence in SAR interferograms in Kiruna, Northern Sweden, *Int. J. Rem. Sens.*, 37, 370–387, 2016.
- Barnett, T., Adam, J., and Lettenmaier, D.: Potential impacts of a warming climate on water availability in snow-dominated regions, *Nature*, 438, 303–309, 2005.
- Belinska, K., Fischer, G., Parrella, G., and Hajnsek, I.: The Potential of Multifrequency Spaceborne DInSAR Measurements for the Retrieval of Snow Water Equivalent, *IEEE JOURNAL OF SELECTED TOPICS IN APPLIED EARTH OBSERVATIONS AND REMOTE SENSING*, 17, 2950–2962, 2024.
- Bonnell, R., Elder, K., McGrath, D., Marshall, H. P., Starr, B., Adebisi, N., Palomaki, R. T., and Hoppinen, Z.: L-Band InSAR Snow Water Equivalent Retrieval Uncertainty Increases With Forest Cover Fraction, *Geophysical Research Letter*, 2024a.
- Bonnell, R., McGrath, D., Tarricone, J., Marshall, H.-P., Bump, E., Duncan, C., Kampf, S., Lou, Y., Olsen-Mikitowicz, A., Sears, M., Williams, K., Zeller, L., and Zheng, Y.: Evaluating L-band InSAR snow water equivalent retrievals with repeat ground-penetrating radar and terrestrial lidar surveys in northern Colorado, 18, 3765–3785, 2024b.
- Conde, V., Nico, G., Mateus, P., Catalão, J., Kontu³, A., and Gritsevich⁴, M.: On the estimation of temporal changes of snow water equivalent by spaceborne SAR interferometry: a new application for the Sentinel-1 mission, *J. Hydrol. Hydromech.*, 67, 93–100, 2019.
- Cui, Y., Xiong, C., Lemmetyinen, J., Shi, J., Jiang, L., Peng, B., Li, H., Zhao, T., Ji, D., and Hu, T.: Estimating Snow Water Equivalent with Backscattering at X and Ku Band on Absorption Loss, *Remote Sensing*, 8, 2016.
- Dagurova, P., Chimitdorzhieva, T., Dmitriev, A., and Dobrynin, S.: Estimation of snow water equivalent from L-band radar interferometry: simulation and experiment, *INTERNATIONAL JOURNAL OF REMOTE SENSING*, 41, 2020.
- Deeb, E. J., Forster, R. R., and Kane, D. L.: Monitoring snowpack evolution using interferometric synthetic aperture radar on the North Slope of Alaska, *Int. J. Remote Sens.*, 32, 3985–4003, 2011.
- DEEMS, J. S., PAINTER, T. H., and FINNEGAN, D. C.: Lidar measurement of snow depth: a review, *Journal of Glaciology*, 59, 467–479, 2013.
- Dozier, J., Bair, E. H., and Davis, R. E.: Estimating the spatial distribution of snow water equivalent in the world’s mountains, *WIREs Water*, 3, 461–474, 2016.
- Durand, M. and Liu, D.: The need for prior information in characterizing snow water equivalent from microwave brightness temperatures, *Remote Sens. Environ.*, 126, 248–257, 2012.
- Engen, G., Guneriussen, T., and Overrein, Y.: Delta-K interferometric SAR technique for snow water equivalent (SWE) retrieval, *IEEE Geosci. Remote Sens. Lett.*, 1, 57–61, 2004.
- Eppler, J., Rabus, B., and Morse, P.: Snow water equivalent change mapping from slope-correlated synthetic aperture radar interferometry (InSAR) phase variations, *The Cryosphere*, 16, 1497–1521, 2022.
- Fleming, S. W., Zukiewicz, L., Strobel, M. L., Hofman, H., and Goodbody, G. G.: SNOTEL, the soil climate analysis network, and water supply forecasting at the natural resources conservation service: Past, present, and future, *JAWRA: Journal of the American Water Resource Association*, 59, 585–599, 2023.



- Gabriel, A. K., Goldstein, R. M., and Zebker, H. A.: Mapping small elevation changes over large areas: Differential radar interferometry, *J. Geophys. Res.*, 94, 9183–9191, 1989.
- Guneriussen, T., Hogda, K. A., Johnsen, H., and Lauknes, I.: InSAR for estimation of changes in snow water equivalent of dry snow, *IEEE Trans. Geosci. Remote Sens.*, 39, 2101–2108, 2001.
- H. Rott, T. N. and Scheiber, R.: Snow mass retrieval by means of SAR interferometry, *Proc. 3rd Fringe Workshop Eur. Space Agency Earth Observ.*, 2003.
- Hoppinen, Z., Oveisgharan, S., Marshall, H. P., Mower, R., Elder, K., and Vuyovich, C.: Snow water equivalent retrieval over Idaho—Part 2: Using L-band UAVSAR repeat-pass interferometry, *The Cryosphere*, 18, 575–592, 2024a.
- Hoppinen, Z., Palomaki, R. T., Brencher, G., Dunmire, D., Gagliano, E., Marziliano, A., Tarricone, J., and Marshall, H.-P.: Evaluating snow depth retrievals from Sentinel-1 volume scattering over NASA SnowEx sites, *The Cryosphere*, 18, 5407–5430, 2024b.
- Hui, L., Pengfeng, X., Xuezhi, F., Guangjun, H., and Zuo, W.: Monitoring Snow Depth And Its Change Using Repeat-Pass Interferometric SAR In Manas River Basin, *IGARSS*, pp. 4936–4939, 2016.
- Jolivet, R., Grandin, R., Lasserre, C., Doin, M., and Peltzer, G.: Systematic InSAR tropospheric phase delay corrections from global meteorological reanalysis data, *GEOPHYSICAL RESEARCH LETTERS*, 38, 2011.
- Kellndorfer, J., Cartus, O., Laval, M., Magnard, C., Milillo, P., Oveisgharan, S., Osmanoglu, B., Rosen, P. A., and Wegmüller, U.: Global seasonal Sentinel-1 interferometric coherence and backscatter data set, *Scientific Data*, 9, 2022.
- Kelly, R.: The AMSR-E Snow depth algorithm: Description and initial results, *J. Remote Sens. Soc. Jpn.*, 29, 307–317, 2009.
- Kelly, R. E., Chang, A. T., Tsang, L., and Foster, J. L.: A prototype AMSR-E global snow area and snow depth algorithm, *IEEE Transactions on Geoscience and Remote Sensing*, 41, 230–242, 2003.
- Klos, P. Z., Link, T. E., and Abatzoglou, J. T.: Extent of the rain-snow transition zone in the western US under historic and projected climate, *Geophys. Res. Lett.*, 41, 4560–4568, 2014.
- Larsen, Y., Malnes, E., and Engen, G.: Retrieval of snow water equivalent with envisat ASAR in a Norwegian hydropower catchment, *Proc. IEEE Int. Geosci. Remote Sens. Symp.*, 8, 5444–5447, 2005.
- Laval, M., Simard, M., and Hensley, S.: A Temporal Decorrelation Model for Polarimetric Radar Interferometers, *IEEE Transactions on Geoscience and Remote Sensing*, 2012.
- Leinss, S., Parrella, G., and Hajnsek, I.: Snow Height Determination by Polarimetric Phase Differences in X-Band SAR Data, *IEEE Journal of Selected Topics in Applied Earth Observations and Remote Sensing*, 7, 3794–3810, 2014.
- Leinss, S., Wiesmann, A., Lemmetyinen, J., and Hajnsek, I.: Snow Water Equivalent of Dry Snow Measured by Differential Interferometry, *IEEE Journal of Selected Topics in Applied Earth Observations and Remote Sensing*, 8, 3773–3790, 2015.
- Lemmetyinen, J., Derksen, C., Rott, H., Macelloni, G., King, J., Schneebeli, M., Wiesmann, A., Leppanen, L., Kontu, A., and Pulliainen, J.: Retrieval of Effective Correlation Length and Snow Water Equivalent from Radar and Passive Microwave Measurements, *Remote Sensing*, 10, 2018.
- Li, D., Wrzesien, M. L., Durand, M., Adam, J., and Lettenmaier, D. P.: How much runoff originates as snow in the western United States, and how will that change in the future?, *Geophys. Res. Lett.*, 44, 6163–6172, 2017.
- Lievens, H., Demuzere, M., Marshall, H.-P., Reichle, R. H., Brucker, L., Brangers, I., de Rosnay, P., Dumont, M., Giroto, M., Immerzeel, W. W., Jonas, T., Kim, E. J., Koch, I., Marty, C., Saloranta, T., Schöber, J., and Lannoy, G. J. D.: Snow depth variability in the Northern Hemisphere mountains observed from space, *Nature Communications*, 10, 2019.



- Lievens, H., Brangers, I., Marshall, H.-P., Jonas, T., Olefs, M., and DeLannoy, G.: Sentinel-1 snow depth retrieval at sub-kilometer resolution over the European Alps, *The Cryosphere*, 16, 159–177, 2022.
- Liu, Y., Li, L., Yang, J., Chen, X., and Hao, J.: Estimating Snow Depth Using Multi-Source Data Fusion Based on the D-InSAR Method and 3DVAR Fusion Algorithm, *Remote Sensing*, 9, 2017.
- 465 Lorenzi, V., F. Banzato, F., Barberio, M., Goepfert, N., Goldscheider, N., Gori, F., Lacchini, A., Manetta, M., Medici, G., Rusi, S., and Petitta, M.: Tracking flowpaths in a complex karst system through tracer test and hydrogeochemical monitoring: Implications for groundwater protection (Gran Sasso, Italy), *Heliyon*, 10, 2024.
- Luzi, G., Noferini, L., Mecatti, D., Macaluso, G., Pieraccini, M., Atzeni, C., Schaffhauser, A., Fromm, R., and Nagler, T.: Using a ground-based SAR interferometer and a terrestrial laser scanner to monitor a snow-covered slope: Results from an experimental data collection in
 470 Tyrol, *IEEE Trans. Geosc. Rem. Sens.*, 47, 382–393, 2009.
- Marshall, H., Deeb, E., Forster, R., Vuyovich, C., Elder, K., Hiemstra, C., and Lund, J.: L-BAND INSAR DEPTH RETRIEVAL DURING THE NASA SNOWEX 2020 CAMPAIGN: GRAND MESA, COLORADO, *IEEE International Geoscience and Remote Sensing Symposium*, pp. 625–627, 2021.
- McCrystall, M. R., Stroeve, J., Serreze, M., Forbes, B. C., and Screen, J. A.: New climate models reveal faster and larger increases in Arctic
 475 precipitation than previously projected, *Nature Communication*, 12, 1216–1228, 2021.
- Nagler, T., Rott, H., Scheiblauer, S., Libert, L., Mölg, N., Horn, R., Fischer, J., Keller, M., Moreira, A., and Kubanek, J.: AIRBORNE EXPERIMENT ON INSAR SNOW MASS RETRIEVAL IN ALPINE ENVIRONMENT, *IGARSS*, pp. 4549–4552, 2022.
- Nghiem, S. V. and Tsai, W. Y.: Global snow cover monitoring with spaceborne Ku:band scatterometer, *IEEE Transactions on Geoscience and Remote Sensing*, 39, 2118–2134, 2001.
- 480 Oveisgharan, S. and Zebker, H.: Estimating Snow Accumulation From InSAR Correlation Observations, *IEEE Transactions on Geoscience and Remote Sensing*, 45, 10–20, 2007.
- Oveisgharan, S., Zink, R., Hoppinen, Z., and Marshall, H. P.: Snow water equivalent retrieval over Idaho – Part 1: Using Sentinel-1 repeat-pass interferometry, *The Cryosphere*, 18, 559–574, 2024.
- Painter, T. and et al.: The Airborne Snow Observatory: Fusion of scanning LiDAR, imaging spectrometer, and physically-based modeling
 485 for mapping snow water equivalent and snow albedo, *Remote Sens. Environ.*, 184, 139–152, 2016.
- Painter, T. H., Berisford, D. F., Boardman, J. W., Bormanna, K. J., Deemsc, J. S., Gehrke, F., Hedrick, A., Joycea, M., Laidlaw, R., Marks, D., Mattmann, C., McGurk, B., Ramirez, P., Richardson, M., Skiles, S. M., Seidel, F. C., and Winstral, A.: The Airborne Snow Observatory: Fusion of scanning lidar, imaging spectrometer, and physically-based modeling for mapping snow water equivalent and snow albedo, *Remote Sensing of Environment*, 184, 139–152, 2016.
- 490 Pulliainen, J. and Hallikainen, M.: Retrieval of regional snow water equivalent from space-borne passive microwave observations., *Remote Sens. Environ.*, 75, 76–85, 2001.
- Rott, H., Yueh, S. H., Cline, D. W., Duguay, C., Essery, R., Haas, C., Heliere, F., Kern, M., Macelloni, G., and Malnes, E.: Cold regions hydrology high-resolution observatory for snow and cold land processes, *Proc. IEEE* 2010, 98, 752–765, 2010.
- Ruiz, J. J., Lemmetyinen, J., Kontu, A., Tarvainen, R., Vehmas, R., Pulliainen, J., and Praks, J.: Investigation of Environmental Effects
 495 on Coherence Loss in SAR Interferometry for Snow Water Equivalent Retrieval, *IEEE TRANSACTIONS ON GEOSCIENCE AND REMOTE SENSING*, 60, 4306 715–4306 715, 2022.
- Shah, R., Xu, X., Yueh, S., Chae, C. S., Elder, K., Starr, B., and Kim, Y.: Remote Sensing of Snow Water Equivalent Using P-Band Coherent Reflection, *IEEE GEOSCIENCE AND REMOTE SENSING LETTERS*, 14, 309–313, 2017.



- Siirila-Woodburn, E. R., Rhoades, A. M., Hatchett, B. J., Huning, L. S., Szinai, J., Tague, C., Nico, P. S., Feldman, D. R., Jones, A. D.,
 500 Collins, W. D., and Kaatz, L.: A low-to-no snow future and its impacts on water resources in the western United States, *Nature Review Earth and Environment*, 2, 800–891, 2021.
- Takala, M., Luojus, K., Pulliainen, J., Derksen, C., and and, J. L.: Estimating northern hemisphere snow water equivalent for climate research through assimilation of space-borne radiometer data and ground-based measurements, *Remote Sensing of Environment*, 115, 3517–3529, 2011.
- 505 Tarricone, J., Webb, R., Marshall, H., Nolin, A., and Meyer, F.: Estimating snow accumulation and ablation with l-band InSAR, *The Cryosphere*, 17, 1997–2019, 2023.
- Ulaby, F. T. and Stiles, W. H.: The active and passive microwave response to snow parameters: 2. Water equivalent of dry snow., *J. Geophys. Res. Oceans* (1978–2012), 85, 1045–1049, 1980.
- Yueh, S. H., Xu, X., Shah, R., Kim, Y., Garrison, J. L., Komanduru, A., and Elder, K.: Remote Sensing of Snow Water Equivalent Using
 510 Coherent Reflection From Satellite Signals of Opportunity: Theoretical Modeling, *IEEE Journal of Selected Topics in Applied Earth Observations and Remote Sensing*, 10, 5529–5540, 2017.
- Yueh, S. H., Shah, R., Xu, X., Stiles, B., and Bosch-Lluis, X.: A Satellite Synthetic Aperture Radar Concept Using P-Band Signals of Opportunity, *IEEE JOURNAL OF SELECTED TOPICS IN APPLIED EARTH OBSERVATIONS AND REMOTE SENSING*, 14, 2796–2816, 2021.
- 515 Yunjun, Z., Fattahi, H., and Amelung, F.: Small baseline InSAR time series analysis: Unwrapping error correction and noise reduction, *Computer and Geoscience*, 133, 5529–5540, 2019.
- Zebker, H. A. and Villasenor, J.: Decorrelation in Interferometric Radar Echoes, *IEEE TRANSACTIONS ON GEOSCIENCE AND REMOTE SENSING*, 30, 950–959, 1992.
- Zebker, H. A., Rosen, P. A., Goldstein, R., Gabriel, A., and L. Werner, C.: On the derivation of coseismic displacement fields using differential
 520 radar interferometry: The Landers earthquake, *J. Geophys. Res. Solid Earth*, 99, 19 617–19 634, 1994.